Fluid Dynamics & Materials Processing

Tech Science Press

DOI: 10.32604/fdmp.2024.046158

ARTICLE

Optimized Design of Bio-Inspired Wind Turbine Blades

Yuanjun Dai[1,4,*], Dong Wang[1], Xiongfei Liu[2] and Weimin Wu[3]

[1]School of Mechanical Engineering, Shanghai DianJi University, Shanghai, 201306, China

[2]School of Information Engineering, Yinchuan University of Science and Technology, Yinchuan, 750000, China

[3]School of Mechanical and Power Engineering, Chongqing University of Science and Technology, Chongqing, 401331, China

[4]School of Aeronautical Mechanical and Electrical Engineering, Chongqing Aerospace Polytechnic, Chongqing, 400021, China

[*]Corresponding Author: Yuanjun Dai. Email: daiyj@sdju.edu.cn

Received: 20 September 2023 Accepted: 22 February 2024 Published: 23 July 2024

ABSTRACT

To enhance the aerodynamic performance of wind turbine blades, this study proposes the adoption of a bionic airfoil inspired by the aerodynamic shape of an eagle. Based on the blade element theory, a non-uniform extraction method of blade elements is employed for the optimization design of the considered wind turbine blades. Moreover, Computational Fluid Dynamics (CFD) is used to determine the aerodynamic performances of the eagle airfoil and a NACA2412 airfoil, thereby demonstrating the superior aerodynamic performance of the former. Finally, a mathematical model for optimizing the design of wind turbine blades is introduced and a comparative analysis is conducted with respect to the aerodynamic performances of blades designed using a uniform extraction approach. It is found that the blades designed using non-uniform extraction exhibit better aerodynamic performance.

KEYWORDS

Airfoil; wind turbines; blade design; CFD

1 Introduction

Wind energy, as a green, pollution-free, and renewable energy source, has gradually become a focus of attention [1,2]. Wind turbine blades are crucial components for converting wind energy into mechanical energy, and their shape design significantly impacts the efficiency of the wind power generation system. Therefore, efficient capture and utilization of wind energy to improve energy conversion efficiency are the key points in wind turbine blade design [3–5]. The design of airfoil and blade design methods for wind turbines are crucial for enhancing aerodynamic performance.

In the aspect of airfoil research, Rose et al. [6] introduced knowledge and technology from biomimetics and conducted numerical studies on the tubercles inspired by the humpback whale (HW) using a straight wing and a swept-back wing configuration. Metin et al. [7], inspired by biological systems in nature, increased aerodynamic performance by adding small wings and annular blades at the wing tip. Yuan et al. [8] proposed improving the aerodynamic performance of wind turbine blades by refining the trailing edge of the airfoil. Wang et al. [9] proposed a multi-objective optimization model that combines maximizing the power coefficient and minimizing the surface area of the blade for variable pitch wind turbines using

a novel airfoil. Wang et al. [10] have established a wind turbine airfoil model based on the Generalized Regression Neural Network (GRNN) and proposed an optimization design method to improve the aerodynamic performance of the airfoil under multiple constraints. Yan et al. [11], focusing on sturgeons, have conducted numerical simulation studies by employing 3D reverse engineering and B-spline curve fitting techniques to establish physical models of both asymmetric and symmetric biomimetic airfoils. Zhao et al. [12] have designed a novel serrated airfoil inspired by owl wings, enhancing the overall performance of the airfoil. Hua et al. [13] and Lanzafame et al. [14] have also conducted research on airfoil designs. In research on optimization design methods for wind turbine blades, Lee et al. [15] examined various design parameters and utilized the second-order response surface method to establish the correlation between the objective function and factors such as chord length and torsion angle in the design calculations. They compared the performance of the optimized blade with the original design and found significant improvements. Rodriguez et al. [16] proposed an integrated optimization methodology for wind turbine blade design by combining computational fluid dynamics (CFD), blade element momentum theory (BEM), and genetic algorithms (GA). Özkan et al. [17] have developed a novel optimization technique called the Artificial Bee Colony algorithm based on Blade Element Momentum theory (ABC-BEM), which has been applied to designing small-scale wind turbine blades. A, Zhu et al. [18] have proposed a multi-objective optimization design method for wind turbine systems based on a tower-blade coupling model, aiming to explore the coupling effect between the tower and blades to improve the performance of wind turbine systems. Zhu et al. [19] proposed a Matlab-based program combined with Ansys to achieve an optimal trade-off between maximum power generation and minimum blade mass in wind turbine design. Zemamou et al. [20] investigated the optimization of traditional Savonius blade design using Bézier curves and transient computational fluid dynamics (CFD) simulations. Zhang et al. [21], Maki et al. [22], Tang et al. [23], among others, have also conducted research on methods for wind turbine blade design.

In-depth research has been conducted on the optimization design of wind turbine blades. However, these studies predominantly focus on either airfoil or blade design methods, with limited research on integrating both. This study applies a bionic airfoil design inspired by an eagle, implementing a non-uniform extraction method of blade elements based on the blade element theory for wind turbine blade optimization.

2 Extraction and Aerodynamic Performance Analysis of the Bionic Airfoil

2.1 Extraction of Biomimetic Airfoil

In nature, birds are the most adept at flying, with their wing shapes evolved through natural processes to achieve outstanding flight capabilities. The wings of the sparrowhawk are formed by a lateral arrangement of airfoil shapes. Through fluttering and clever utilization of aerodynamic principles, they generate upward lift and thrust to propel the body forward, resembling the operating conditions of wind turbines. This study employs a portable 3D scanner to scan the sparrowhawk airfoils and acquire a point cloud image. The resulting scan data is processed using image processing software called ImageWare, as illustrated in Fig. 1. To capture the optimal cross-sectional airfoil, multiple interceptions and selections of airfoils were performed. Firstly, cross-section 1 was selected as the reference, and relevant parameters were set. The sparrowhawk airfoil model was divided equally at specified intervals, resulting in a total of 60 intercepted airfoils. Through a comparative analysis, the airfoil located 72 mm from cross-section 1 was identified as the most suitable. Subsequently, cross-section 2 was created for further optimization, with corresponding parameters set and the reference position placed at −72.0 mm. Twenty airfoils were intercepted in this process, and after comparison, the airfoil positioned −73.25 mm from cross-section 1 was found to better meet the conditions. Moving forward, cross-section 3 was created to refine the selection. With predefined parameters, the cross-section position was set at −73.25 mm, and 20 airfoils with a spacing of 0.1 mm were intercepted. After comparison, the airfoil at −73.05 mm from cross-section 1 was determined as the

optimal choice, as shown in Fig. 2. The coordinates of the sparrowhawk airfoil were exported from Geomagic Studio to Profili software for the establishment of the biomimetic airfoil model, as illustrated in Fig. 3.

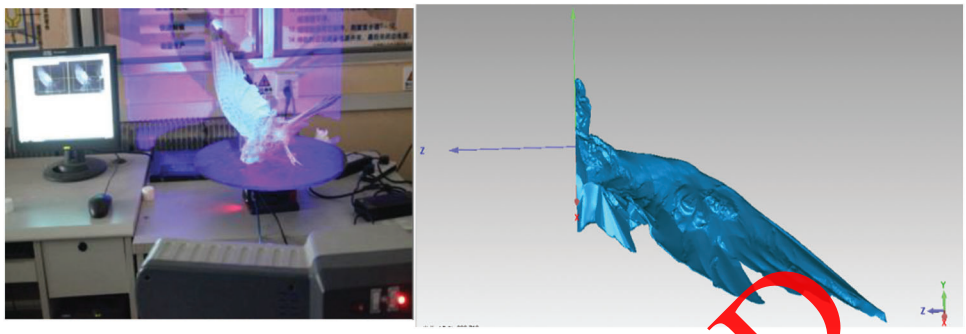

Figure 1: Sparrowhawk airfoil scanning process

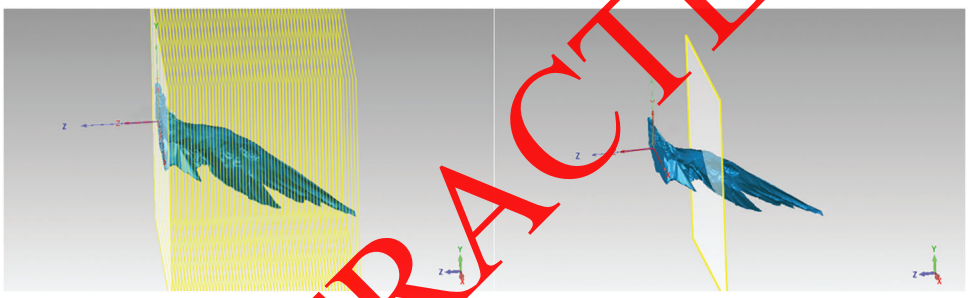

Figure 2: Extraction process of sparrowhawk airfoil type

Figure 3: Sparrowhawk airfoil type QY-7305

Lastly, the final selected sparrowhawk airfoil section was derived, and the collection and fitting of coordinate points were carried out. Using Matlab software, the upper and lower airfoil profiles were fitted to obtain the coordinate equation of the airfoil. The resulting equation is presented below:

Upper wing type:

$$Y_1 = 0.0006x^3 - 0.0367x^2 + 1.1094x + 1.1985 \quad (1)$$

Lower wing type:

$$Y_2 = -0.011x^3 + 0.045x^2 - 0.3793x - 1.3623 \quad (2)$$

The airfoil is named QY-7305, where "QY" represents the initial capitalization of the Chinese name of the Sparrowhawk and "7305" indicates the cross section at −73.05 mm with the characteristic plane as the reference.

2.2 Numerical Computation and Analysis of Airfoil

2.2.1 Modeling and Mesh Generation

Mesh generation of the airfoil was conducted using the ICEM-CFD software, employing a structured grid. The computational domain was defined as a circular region with the leading edge of the airfoil as the center and a radius equal to 10 times the airfoil chord length. The first layer height of the mesh on the airfoil surface was set to 2.2×10^{-5}, with a boundary layer consisting of 10 layers. The wall mesh growth rate was set at 1.1. These conditions were maintained for mesh independent verification, ensuring that variations in cell size did not impact the accuracy of the computational results. Tables 1 and 2 present the influence of different mesh cell numbers on the lift coefficient for the QY-7305 and NACA2412 airfoils at an angle of attack of 6°. It is noted that all cases listed in the tables satisfied the condition of $y+$ being less than 1.

Table 1: Mesh-independent verification (QY-7305)

No.	Number of grids	Lift coefficient	Correlation error %
1	63942	1.5133	1.836
2	78635	1.5369	0.305
3	87985	1.5389	0.175
4	95960	1.5408	0.05
5	11658	1.5416	0

Table 2: Mesh-independent verification (NACA2412)

No.	Number of grids	Lift coefficient	Correlation error %
1	59689	0.7058	2.16
2	73659	0.7125	1.23
3	85460	0.7189	0.346
4	93567	0.7201	0.18
5	10563	0.7214	0

The total number of grids for the selected QY-7305 and NACA2412 airfoils in this study were 95960 and 93567, respectively. The mesh distribution of the QY-7305 airfoil is shown in Fig. 4, and the mesh distribution of the NACA2412 airfoil is shown in Fig. 5.

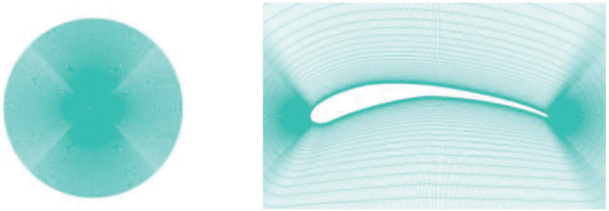

Figure 4: QY-7305 airfoil overall grid and local grid diagram

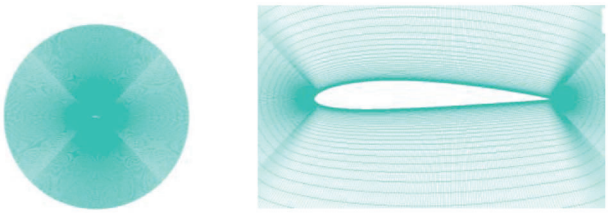

Figure 5: NACA2412 airfoil overall grid and local grid diagram

2.2.2 Numerical Method

The study of the aerodynamic characteristics of wind turbine airfoils is essentially an investigation into the impact of turbulent flow on the aerodynamic properties of wind turbine airfoils. Turbulence is a complex and highly nonlinear flow, requiring a comprehensive understanding of numerical methods for turbulence computation to better simulate and predict various performance aspects of wind turbine airfoils. Considering the balance between computational accuracy and resource requirements, this paper adopts a method based on the Reynolds-Averaged Navier-Stokes approach. The flow velocity studied in this paper is lower than the Mach number of 0.3. Considering the influence of viscous forces, it is simulated as a steady-state incompressible flow.

Continuity equation:

$$\frac{\partial \overline{U_i}}{\partial x_i} = 0 \tag{3}$$

Momentum equation:

$$\frac{\partial \overline{U_i U_j}}{\partial x_i} = \frac{1}{\rho}\frac{\partial \overline{P}}{\partial x_i} + v\frac{\partial \overline{U_i}}{\partial x_i x_j} - \frac{\partial \overline{U'_i U'_j}}{\partial x_j} \tag{4}$$

Reynolds stress tensor equation:

$$\overline{U'_i U'_j} = v_t\left(\frac{\partial \overline{U_i}}{\partial x_j} + \frac{\partial \overline{U_j}}{\partial x_i}\right) - \frac{2}{3}k\delta_{ij} \tag{5}$$

$$k = \frac{1}{2}\overline{U'_i U'_j} \tag{6}$$

In the equation, $\overline{U_i U_j}$ respectively represent the velocity vectors in the i and j directions, P is the fluid pressure, ρ is the air density, and $\overline{U'_i U'_j}$ is the Reynolds stress term generated by the motion of the fluid unit mass. v_t is the vortex viscosity coefficient. δ_{ij} is Kronecker delta.

$$\omega = \varepsilon/k \tag{7}$$

The *SST* $k-\omega$ model is a variant of the Shear-Stress Transport turbulence model used for simulating turbulent flow fields. This model combines two different types of turbulence models, namely the $k-\varepsilon$ model and the $k-\omega$ model, to achieve better performance in different flow regions. The *SST* $k-\omega$ model introduces a correction term near the wall to enhance the accuracy of capturing turbulence structures in the vicinity of the wall. The equations for this model are as follows:

$$\begin{aligned}
&\frac{\partial}{\partial t}(\rho k) + \frac{\partial}{\partial x_i}(\rho k \mu_i) = \frac{\partial}{\partial x_j}\left(\Gamma_k \frac{\partial k}{\partial x_j}\right) + G_k - Y_k + S_k \\
&\frac{\partial}{\partial t}(\rho \omega) + \frac{\partial}{\partial x_i}(\rho \omega \mu_i) = \frac{\partial}{\partial x_j}\left(\Gamma_\omega \frac{\partial \omega}{\partial x_j}\right) + G_\omega - Y_\omega + S_\omega
\end{aligned} \tag{8}$$

$$G_k = -\rho\overline{U'_i U'_j}\frac{\partial U_j}{\partial x_i} \tag{9}$$

$$G_\omega = -\rho\frac{\omega\alpha}{k}\overline{U'_i U'_j}\frac{\partial U_j}{\partial x_i} \tag{10}$$

$$Y_k = \rho\beta^* f_\beta \cdot k\omega \tag{11}$$

$$Y_\omega = \rho\beta_i f_\beta \cdot \omega^2 \tag{12}$$

$$\beta_i = F_1\beta_{i,1} + (1 - F_1)\beta_{i,2} \tag{13}$$

$$\Gamma_k = \mu + \frac{\mu_t}{\sigma_k} \tag{14}$$

$$\Gamma_\omega = \mu + \frac{\mu_t}{\sigma_\omega} \tag{15}$$

$$\sigma_k = \frac{1}{F_1/\sigma_{k,1} + (1 - F_1)/\sigma_{k,2}} \tag{16}$$

$$\sigma_\omega = \frac{1}{F_1/\sigma_{\omega,1} + (1 - F_1)/\sigma_{\omega,2}} \tag{17}$$

The turbulent viscosity is calculated as follows:

$$\mu_t = \rho\frac{\alpha^* k}{\omega} \tag{18}$$

In the equations, G_k and G_ω represent the generation terms of turbulence kinetic energy due to the mean velocity gradients, Γ_k and Γ_ω are the effective diffusivity coefficients for k and ω, Y_k and Y_ω denote the dissipation terms due to turbulence, S_k and S_ω is a user-defined source term. The Constant coefficients in the *SST* $k - \omega$ model are shown in Table 3.

Table 3: Constant coefficients in the SST $k - \omega$ model

Model constants	Value
α*	1
α	0.52
β*	0.09
$\beta_{i,1}$	0.075
$\beta_{i,2}$	0.0828
$\sigma_{k,1}$	1.176
$\sigma_{k,2}$	1
$\sigma_{\omega,1}$	2
$\sigma_{\omega,2}$	1.168

The airfoil surface is set as a no-slip wall boundary, and the boundary conditions for the domain are chosen using a pressure far-field approach. The incoming flow velocity is adjusted by changing the Mach number setting. The angle of attack is altered by modifying the X and Y components of the incoming flow direction. The present study employs a pressure-based algorithm and a second-order upwind differencing scheme for discretization, using the SIMPLE pressure-velocity coupling method with double-precision solving. During the solving process, in addition to monitoring the residuals of the variables, lift coefficient (C_L), and drag coefficient (C_D) must also be tracked to ensure true convergence of the solution. The convergence criteria for all calculations are residuals less than 1×10^{-5} [24,25].

2.2.3 Analysis of Computational Results

The analysis focuses on varying the incoming angle of attack, specifically examining the range of 0–12 degrees in this paper. As shown in Fig. 6, the pressure distributions on the QY-7305 airfoil are presented for angles of attack of 0°, 6°, and 12°. Similarly, Fig. 7 illustrates the pressure distributions on the NACA2412 airfoil at angles of attack of 0°, 6°, and 12°. Taking the 0° angle of attack as an example, the pressure on the upper surface of the QY-7305 airfoil is approximately −106 Pa, while the pressure on the lower surface is around 24 Pa, resulting in a pressure difference of 130 Pa. On the other hand, the NACA2412 airfoil exhibits a pressure of about −45 Pa on the upper surface and approximately 2 Pa on the lower surface. Consequently, the pressure difference amounts to approximately 47 Pa for the NACA2412 airfoil. Notably, at a 0° angle of attack, the QY-7305 airfoil displays a larger pressure difference, indicating higher lift.

Figure 6: Pressure clouds of QY-7305 airfoil at angles of attack of 0°, 6° and 12°

Figure 7: Pressure clouds of NACA2412 airfoil at angles of attack of 0°, 6° and 12°

The lift-to-drag ratio is a key metric for assessing the aerodynamic performance of an airfoil. As shown in Fig. 8, it illustrates the characteristic curve of the lift-to-drag ratio for the QY-7305 and NACA2412 airfoils across angles of attack from 0 to 12 degrees. Analyzing the lift-to-drag ratio characteristic curve provides insights into the aerodynamic performance of the airfoils. In the graph, it is evident that the lift-to-drag ratio of the QY-7305 airfoil is higher than that of the NACA2412 airfoil at the optimal angle of attack. Additionally, the QY-7305 airfoil maintains a superior lift-to-drag ratio over a broader range of angles of attack compared to the NACA2412 airfoil, indicating better aerodynamic performance for the QY-7305 airfoil.

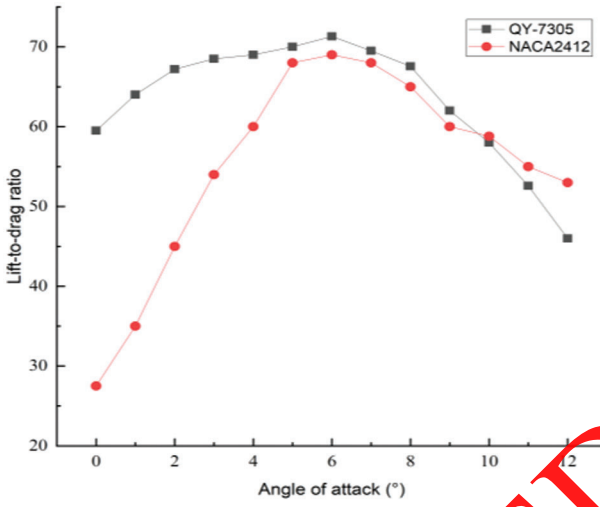

Figure 8: Comparative analysis of lift-to-drag ratio of airfoil

3 Aerodynamic Profile Design of Wind Turbine Blades

The key design parameters for wind turbine blades include the selection and design of the blade airfoil, the number of blades (B), the blade diameter (D), the design wind speed (V), the chord length (C), and the twist angle (θ). These parameters collectively determine the performance characteristics of the blades.

3.1 Determination of the Overall Parameters of the Wind Turbine

The design parameters of the wind turbine in this paper are shown in Table 4. The wind turbine's rated power is custom set to 44 kW, with a transmission efficiency and wind energy utilization coefficient of 0.85 and 0.40 respectively. The incoming wind speed is 12 m/s, and the airfoil is chosen as the QY-7305. For small wind turbines, the typical tip speed ratio is between 3–7. In this study, a tip speed ratio of 6 is selected. For tip speed ratios within the range of 5–8, the number of blades for the wind turbine is chosen between 2–4. In this study, 3 blades are selected.

Table 4: Design parameters of wind turbine blades

Rated power (kW)	Wind turbine drive efficiency $\eta 1 \times \eta 2$	Wind energy utilization factor C_P	Air density (kg/m³)	Design wind speed (m/s)	Number of blades B	Blade tip speed ratio $\lambda 0$	Airfoil type
44	0.85	0.40	1.225	12	3	6	QY-7305

The diameter of the wind turbine can be determined using the following equation for power of the airfoil:

$$P = \frac{1}{2}\pi\rho\eta Cp\left(\frac{D^2}{4}\right)V^3 \tag{19}$$

obtained by transforming Eq. (19):

$$D = \sqrt{\frac{8P}{\pi\rho\eta CpV^3}} = \sqrt{\frac{8 \times 44000}{\pi \times 1.225 \times 0.85 \times 0.4 \times 12^3}} = 12.5\,(m)$$

It is calculated that the diameter of wind wheel $D = 12.5$ m, the hub of wind turbine is taken as 0.5 m, and the radius of wind wheel is taken as $R = 6$ m.

3.2 Establish the Mathematical Model of Blade Optimization Design Method

The Wilson design method, which is based on the blade element theory, divides the blade into equal sections and uses the maximum power coefficient of each section as the objective function for optimization and solution. Increasing the number of segmented elements in the Wilson design method leads to more element cross sections being aligned with the objective function, resulting in a wind turbine blade design that closely approaches an optimal shape and exhibits improved aerodynamic performance. Excessive elements complicate the calculation and modeling process, while insufficient elements compromise accuracy and lead to errors in fitting chord length and twist angle, thereby affecting the optimization of wind turbine blade shape design. This paper proposes a method for non-uniformly acquiring wind turbine blade elements, enabling the adjustment of element numbers within an optimal range to achieve high calculation accuracy. This approach facilitates the creation of 3D models and enhances wind turbine energy utilization. Additionally, relevant correction functions are employed to rectify the calculated element twist angle and element chord length parameters, thereby providing greater convenience for wind turbine blade design based on the easy 3D model generation.

The basic mathematical model for pneumatic shape calculation is as follows:

To maximize the wind energy utilization factor of the entire wind turbine, the wind energy utilization factor of each blade section must be maximized, where the objective function is:

$$dCp = \frac{8}{\lambda_0^2}(1-a)bF\lambda^3 d\lambda \tag{20}$$

The constraints for this objective function is:

$$a(1-aF) = b(1+b)\lambda^2 \tag{21}$$

where:

$$F = \frac{2}{\pi}\arccos(e^{(-f)}) \tag{22}$$

$$f = \frac{B}{2}\frac{R-r}{R\sin\varphi} \tag{23}$$

After obtaining the induced factors a and b, the chord length C and the installation angle can be obtained by the follo airfoil equation θ:

$$\tan\varphi = \frac{(1-a)}{(1-b)}\frac{1}{\lambda} \tag{24}$$

$$\theta = \varphi - \alpha \tag{25}$$

$$\frac{BCC_L}{r} = \frac{8\pi aF\sin^2\varphi}{\cos\varphi}\frac{(1-aF)}{(1-a)^2} \tag{26}$$

$$Re = \frac{V(1-a)C}{\mu\sin\mu} \tag{27}$$

In the above formulas, C_P is the wind energy utilization coefficient, a is the axial induction factor, b is the tangential induction factor, F is the tip loss factor, B is the number of blades, r is the distance from the

blade element cross-section to the rotor center, φ is the inflow angle, α is the angle of attack, θ is the twist angle, V is the incoming wind speed, C is the chord length, C_L is the lift coefficient, μ is the dynamic viscosity, and the dynamic viscosity is set to 1.385×10^{-5} m^2/s.

Firstly, according to the blade element theory, the wind turbine blade is divided into three parts along the spreading direction, which are blade root, blade middle and blade tip. The spacing between the blade elements at the root is 1.2 m, divided into two equal parts; the spacing between the blade elements at the middle of the blade is 0.3 m, divided into nine equal parts; the spacing between the blade elements at the tip is 0.9 divided into one equal part; each blade element is a separate airfoil that needs to be calculated.

For each blade element, the optimization problem is solved using Eq. (20) as the objective function and (21)–(23) as the constraints to determine the induced factors "*a*" and "*b*" of the blade element cross section, as well as the slight blade loss factor "*F*".

A fitting function is employed to fit the best lift coefficients for different Reynolds numbers to a curve. Using the initial Reynolds number, the initial lift coefficient and chord length are calculated based on Eq. (26).

The fitting function is called to fit the best angle of attack corresponding to different Reynolds numbers to a curve, and according to Eq. (27), the Reynolds number is calculated to obtain the best angle of attack by fitting the fitted curve, and the twist angle is obtained by Eq. (28).

The obtained chord lengths and twist angles are ideal, so it is necessary to make linear corrections to the obtained chord lengths and twist angles in order to make the blades meet the requirements of machining, structure, etc.

Obtain the 3D coordinates of the airfoil sections of each blade element and import the 3D coordinates into Solidworks for modeling.

4 Programming and Computation

The program is developed using the Wilson optimization design method, and the optimization flowchart is presented in Fig. 9.

In the programming, it is important to divide it into three parts: blade root, blade middle, and blade tip. Within the entire loop, if statements are inserted. After calculating the blade root, the various parameters are iterated to calculate the blade middle to prevent inaccurate results due to re-iteration. Similarly, after calculating the blade middle, the parameters are iterated to calculate the blade tip. This process continues until the calculation for the entire blade element is completed.

The ideal wind energy utilization coefficient for each cross-section of the blade element is presented in Fig. 10. It can be observed that the wind energy utilization coefficient at each cross-section falls within the Baez limit of 0.593. The position where the blade primarily generates power is towards the middle. Moreover, the C_P (coefficient of power) at the middle position of the blade exceeds 0.5, and C_{Pmax} (maximum coefficient of power) is almost above 0.55, which is very close to the Baez limit. Meanwhile, the program output, which characterizes whether the Fmincon function finds the optimal value under the given constraint, indicates successful program execution after computing the optimal value.

The iterative calculations result in optimized chord lengths and twist angles for each blade element, maximizing the utilization of wind energy. However, in this ideal state, the chord length and twist angle exhibit a nonlinear relationship along the length of the blade, posing challenges in production and processing. To meet the design requirements for production and processing, it is necessary to utilize the curve-fitting function Polyfit in Matlab to perform fitting operations on the optimized chord lengths and twist angles. If the fitting iterations are too low, it may result in a significant deviation from the optimized

parameters, reducing wind energy utilization. On the other hand, higher fitting iterations may approach theoretical data, but they might not achieve the desired correction effect, making installation and manufacturing more inconvenient. After comprehensive consideration and practical analysis, a third-degree polynomial fitting is applied to correct both the chord length and twist angle in this project. Due to the lower wind energy utilization at the blade root and tip, the chord length and twist angle of each blade element section within the range of 0.4 R–0.9 R are subjected to fitting correction. Moreover, at 0.4 R–0.9 R, the blade elements are positioned in the middle of the blade with small spacing, leading to a better fitting effect. The curves in Fig. 11 depict the chord length and twist angle after fitting correction. Through the analysis of the curves, it can be observed that the fitting results ensure a smooth transition in the chord length at the blade tip, and excessive twist angles at the blade root are corrected.

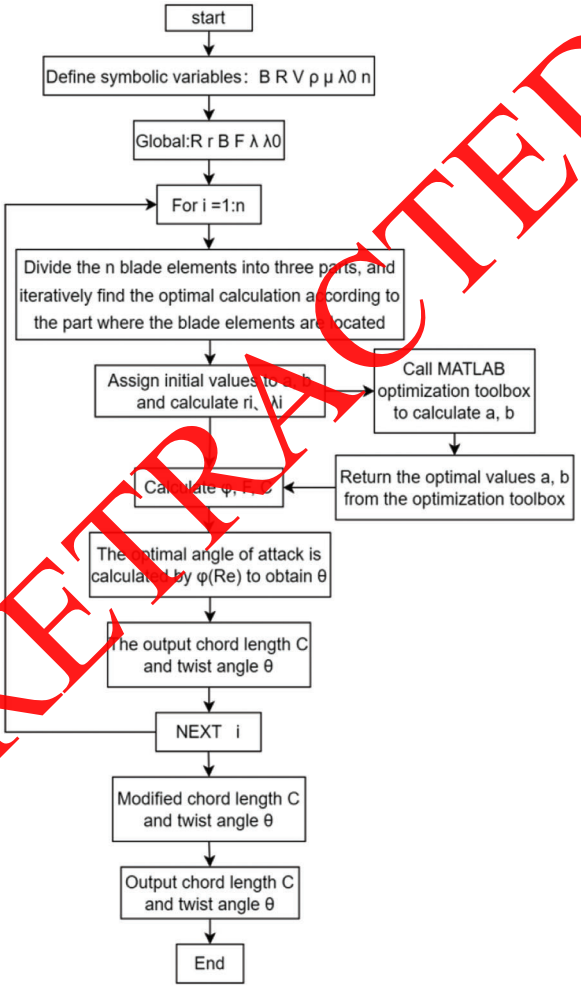

Figure 9: Program flow chart

Fitting polynomial for the chord length:

$$C(r) = -0.003518r^3 + 0.05453r^2 - 0.325r + 0.9038 \tag{28}$$

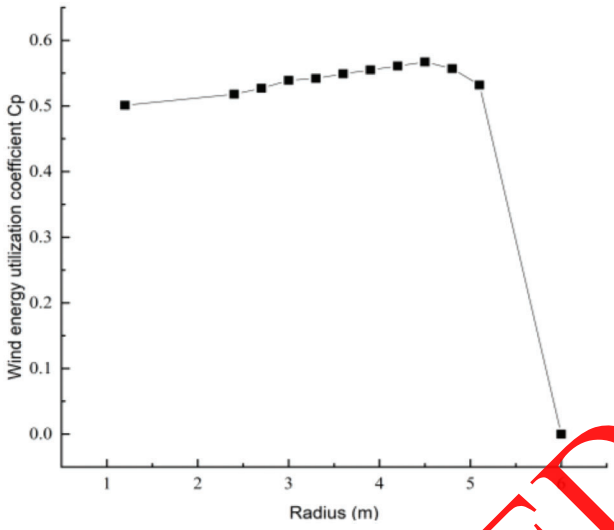

Figure 10: Variation of wind energy utilization coefficient along the radius

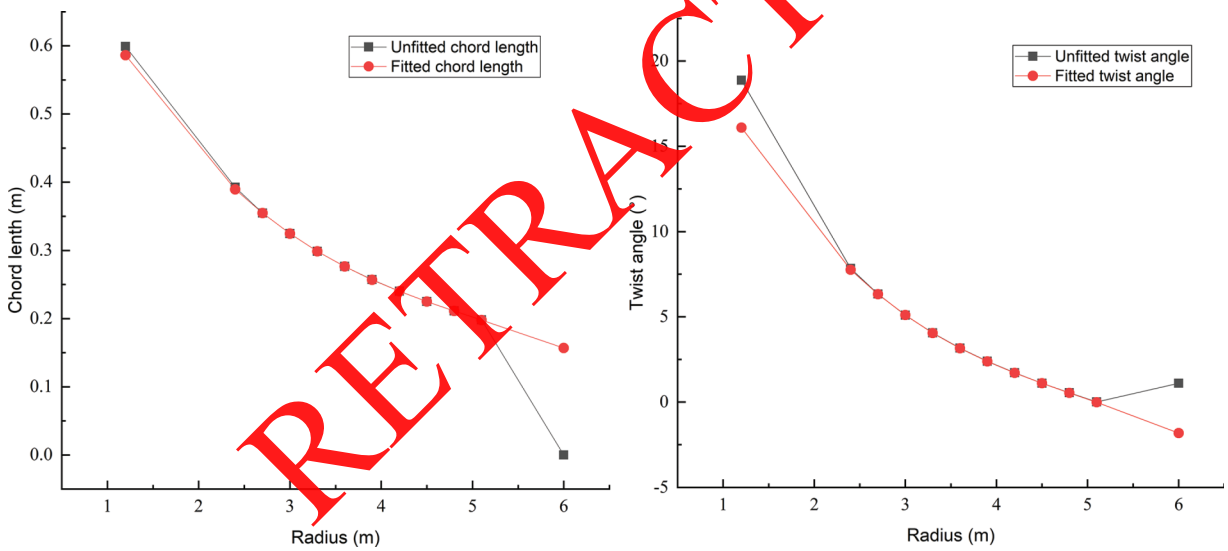

Figure 11: Chord length and twist angle fitting curve graph

Fitting polynomial for the twist angle:

$$\theta(r) = -0.1673r^3 + 2.498r^2 - 14.25r + 29.89 \tag{29}$$

The optimized values of each prime surface parameter for the blades are presented in Table 5.

5 3D Modeling of the Blade

The wind turbine blade is a vital component of the wind turbine, and its complex shape poses challenges in achieving accurate modeling. The accuracy of the modeling directly impacts the efficiency of wind energy utilization.

Table 5: Parameters of each blade element cross-section of the blade

Radius/m	*a*	*b*	Twist angle/°	Fitting twist angle/°	Chord length/m	Fitting chord length/m	*F*	*Re*
1.2	0.3351	0.1422	18.88	16.10	0.5990	0.5862	0.9593	790613
2.4	0.3393	0.0387	7.84	7.77	0.3924	0.3893	0.9810	876708
2.7	0.3398	0.0308	6.34	6.33	0.3547	0.3546	0.9822	878994
3	0.3405	0.0251	5.10	5.10	0.3246	0.3246	0.9822	884600
3.3	0.3414	0.0209	4.06	4.06	0.2988	0.2987	0.9811	888609
3.6	0.3427	0.0177	3.17	3.16	0.2765	0.2764	0.9787	891745
3.9	0.3446	0.0152	2.40	2.39	0.2572	0.2570	0.9744	894175
4.2	0.3473	0.0133	1.72	1.71	0.2402	0.2401	0.9673	895912
4.5	0.3513	0.0118	1.11	1.10	0.2250	0.2250	0.9554	896697
4.8	0.3574	0.0107	0.55	0.54	0.2113	0.2111	0.9351	895710
5.1	0.3669	0.0099	0.01	0.00	0.1981	0.1980	0.8989	890634
6	0.1419	0.0039	1.11	−1.82	0.0000	0.1570	0.0000	0

By using the method of coordinate transformation, we first export the two-dimensional coordinates of each blade element section in Profili software, and then use the formula for spatial coordinate transformation to calculate the three-dimensional spatial coordinates of each blade element section. Finally, we import the three-dimensional coordinates of each blade element section into the modeling software to complete the modeling process. The basic process of coordinate transformation and the specific steps for solving three-dimensional coordinates are as follows:

(1) Obtain the raw airfoil coordinates (x_0, y_0) using Profili software.

(2) The acquired cross-section will be translated to the aerodynamic center, enabling the determination of two-dimensional coordinates (x_1, y_1). The coordinates of the aerodynamic center are assumed to be $(0.25C, 0)$. $(x_1, y_1) = (x_0, y_0) - (0.25C, 0)$.

(3) Through the implementation of a three-dimensional coordinate transformation, the resulting coordinates are (x, y, z).

$$\begin{aligned} x &= C \times \sqrt{x_1^2 + y_1^2} \times cos\left(arctg\frac{y_1}{x_1} + \theta\right) \\ y &= C \times \sqrt{x_1^2 + y_1^2} \times sin\left(arctg\frac{y_1}{x_1} + \theta\right) \\ z &= r \end{aligned} \tag{30}$$

The calculated coordinates of each airfoil section are saved, and then imported into SolidWorks for the purpose of modeling. The resulting 3D model of the wind turbine is presented in Fig. 12.

6 Analysis and Discussion of Aerodynamic Performance Calculation Results

6.1 Aerodynamic Parameter Calculation Results

Aerodynamic performance calculation plays a crucial role in blade design and verification processes. Verifying its aerodynamic performance becomes an essential step to evaluate the design outcomes. Conversely, the results obtained from aerodynamic performance calculations offer valuable feedback for refining the aerodynamic shape of the blade.

Figure 12: 3D model of the wind turbine

In this study, the aerodynamic performance parameters are computed using the fitting formulas for chord length and twist angle obtained through the non-uniformly sampled blade element method. Additionally, a comparison is performed using the uniformly sampled blade element method for analysis. Both methods utilize twelve cross-sectional blade elements to calculate each parameter, with chord length and twist angle corrections made at 0.4 R–0.9 R. The chord length and twist angle functions obtained through fitting using two methods are used to calculate the aerodynamic performance parameters, including the wind energy utilization coefficient (C_P), torque coefficient (C_M), and thrust coefficient (C_T). The curve depicting the variation of C_P with tip speed ratio is shown in Fig. 13, the curve depicting the variation of C_M with tip speed ratio is shown in Fig. 14, and the curve depicting the variation of C_T with tip speed ratio is shown in Fig. 15.

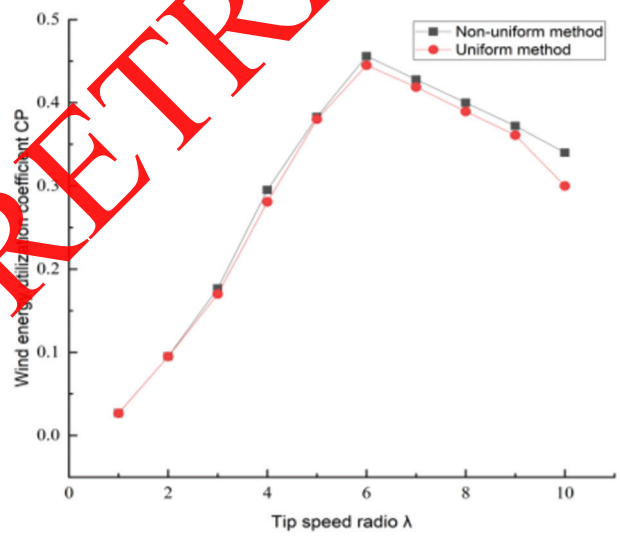

Figure 13: C_P with tip speed ratio

6.2 Comparative Analysis of Aerodynamic Parameter Results

Figs. 13–15 illustrate that the calculated wind energy utilization coefficient (C_P) reaches maximum values of 0.4614 and 0.4516 when designing wind turbine blades using the non-uniform and uniform blade element methods, respectively, at a tip speed ratio of 6. Similarly, the torque coefficient (C_M) reaches values of 0.0769 and 0.0752, while the thrust coefficient (C_T) reaches values of 0.801 and 0.755.

The wind energy utilization coefficient (C_P) holds utmost significance for assessing the aerodynamic performance of wind turbine blades, reflecting their efficiency in capturing wind energy. Within the tip speed ratio range of 5 to 10, the wind energy utilization coefficient calculated using the non-uniform blade element method consistently surpasses that of the uniform blade element method. Additionally, it aligns with the tip speed ratio at the design point, attaining its peak value when the tip speed ratio is 6. Consequently, designing blades using the non-uniform blade element method leads to enhanced aerodynamic performance.

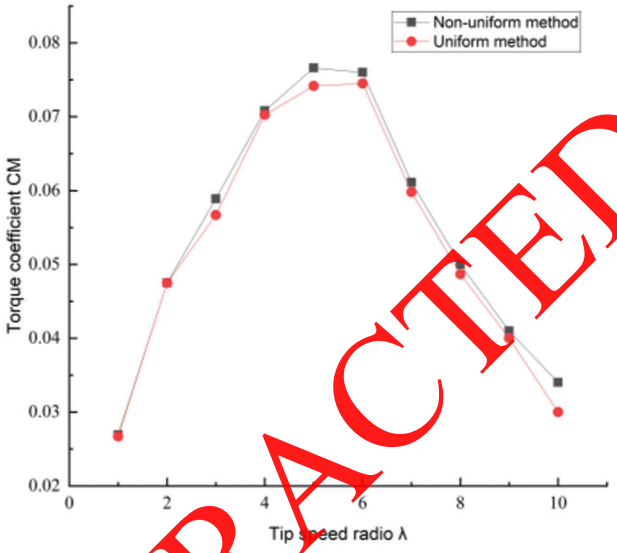

Figure 14: C_M with tip speed ratio

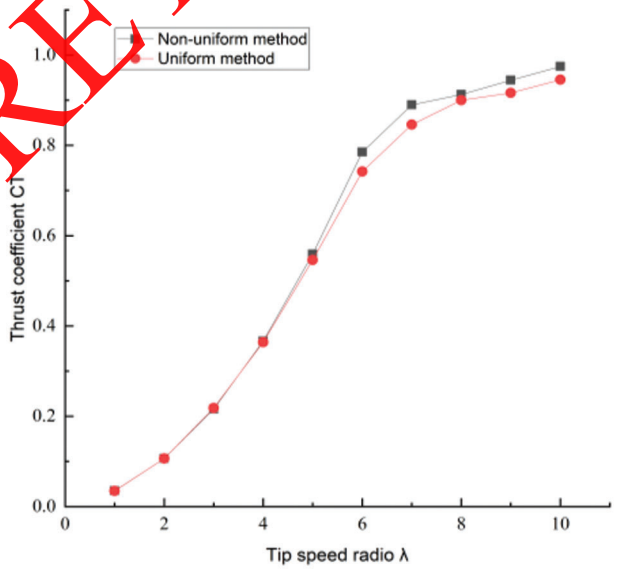

Figure 15: C_T with tip speed ratio

This study utilized two distinct methods for conducting calculations and analysis in wind turbine design. Specifically, 10, 15, 20, and 30 blade elements were employed, and the resulting outcomes are presented in Table 6. The findings demonstrate that the non-uniform blade element method surpasses the uniform blade element method in terms of aerodynamic performance calculations when a smaller number of blade elements is used. However, when a larger number of blade elements is employed, the calculated aerodynamic performance parameters are essentially the same for both methods. This is primarily due to the fact that with a larger number of blade elements, both methods exhibit greater accuracy in fitting the chord length and twist angle within the 0.4 R–0.9 R range. In contrast, when fewer blade elements are utilized, the non-uniform blade element method achieves a smaller spacing between blade elements within the 0.4 R–0.9 R range, thereby enabling higher precision in fitting the chord length and twist angle and resulting in more accurate aerodynamic performance calculations. Consequently, employing the non-uniform blade element method not only yields superior aerodynamic performance for the geometric shape of wind turbine blades, but also circumvents the issue of excessive blade elements, which can lead to cumbersome calculations and modeling.

Table 6: Aerodynamic calculation results of different blade elements

Number of blade elements	10	12	15	20	30
Wind energy utilization coefficient obtained through non-uniform design method	0.4588	0.4614	0.4621	0.4622	0.4623
Wind energy utilization coefficient obtained through uniform design method	0.4472	0.4516	0.4596	0.4617	0.4621

7 Conclusion

In this study, we extracted an airfoil inspired by the eagle and employed it in conjunction with the non-uniform blade element method to enhance the design of wind turbine blades. The resulting conclusions are outlined below:

(1) Using biomimicry, the airfoil of an eagle was extracted and compared with the aerodynamic characteristics of the NACA2412 airfoil. Through the analysis, it was determined that the eagle airfoil demonstrated superior aerodynamic performance.

(2) The blade was designed using the non-uniform blade element method and then compared with the same method itself. The analysis showed that the blades designed using this approach demonstrated superior aerodynamic performance, while effectively mitigating the challenge of increased complexity in calculations and modeling arising from a higher number of blade elements.

(3) When a smaller number of blade elements is used, the non-uniform blade element method outperforms the uniform blade element method.

Acknowledgement: None.

Funding Statement: This study was supported by the National Natural Science Foundation Projects (Grant Number 51966018), the Chongqing Natural Science Foundation of China (Grant Number cstc2020jcyj-msxmX0314), the Key Research & Development Program of Xinjiang (Grant Number 2022B01003), Ningxia Key Research and Development Program of Foreign Science and Technology Cooperation Projects (202204), and the Key Scientific Research Project in Higher Education Institution from the Ningxia Education Department (2022115).

Author Contributions: The authors confirm contribution to the paper as follows: supervision, project administration, funding acquisition and writing-review & editing: Yuanjun Dai, Dong Wang, Xiongfei Liu, Weimin Wu; study conception and design: Yuanjun Dai, Dong Wang; data collection: Dong Wang; analysis and interpretation of results: Dong Wang; draft manuscript preparation: Dong Wang. All authors reviewed the results and approved the final version of the manuscript.

Availability of Data and Materials: The authors confirm that the data supporting the findings of this study are available within the article.

Conflicts of Interest: The authors declare that they have no conflicts of interest to report regarding the present study.

References

1. Mitchell S, Ogbonna I, Volkov K. Improvement of self-starting capabilities of vertical axis wind turbines with new design of turbine blades. Sustain. 2021;13(7):3854–24.
2. Gen MS, Zkan R. Optimum layer sequence analysis for composite blade using ACP-FSI model. Int J Sust Aviat. 2021;7(4):354–17.
3. Zhang J, Yang SU, Yong LI, Cong X. Numerical study on the flow control of vortex generators on large wind turbine blades. Int J Intell Energy. 2021;43(12):66–5.
4. Muhsen H, Al-Kouz W, Khan W. Small wind turbine blade design and optimization. Symmetry. 2019;12(1):18–4.
5. Tarfaoui M, Shah OR, Nachtane M. Design and optimization of composite offshore wind turbine blades. J Energy Resour Technol. 2019;141(5):051204–9.
6. Rose JBR, Natarajan SG, Gopinathan VT. Biomimetic flow control techniques for aerospace applications: a comprehensive review. Rev Environ Sci Biotechnol. 2021;20(3):645–32.
7. Metin U, Özdemir M, Yildirim ÇV, Çoban S. A novel biomimetic wing design and optimizing aerodynamic performance. J Aviat. 2022;6(1):12–3.
8. Yuan SK, Li RN. Analysis influence of trailing edge modification on aerodynamic performance of airfoils for wind turbine. Appli Mechanic Materi. 2012;220–223(2):900–4.
9. Wang Q, Wang J, Chen J, Lou S, Sun J. Aerodynamic shape optimized design for wind turbine blade using new airfoil series. J Mech Sci Technol. 2015;29(7):2871–11.
10. Wang X, Ju H, Lu J. Wind turbine airfoils optimization design by generalized regression neural network under small sample. J Mech Sci Technol. 2023;37(1):217–11.
11. Yan H, Su X, Zhang H, Hang J, Zhou L, Liu Z, et al. Design approach and hydrodynamic characteristics of a novel bionic airfoil. Ocean Eng. 2020;216(8):108076–10.
12. Zhao M, Cao H, Zhang M, Liao C, Zhou T. Optimal design of aeroacoustic airfoils with owl-inspired trailing-edge serrations. Bioinspir Biomim. 2021;16(5):056004–14.
13. Hua X, Zhang C, Wei J, Hu X, Wei H. Wind turbine bionic blade design and performance analysis. J Vis Commun Image R. 2019;60(3):258–7.
14. Lanzafame R, Messina M. Design and performance of a double-pitch wind turbine with non-twisted blades. Renew Energy. 2009;34(5):1413–7.
15. Lee SL, Shin SJ. Wind turbine blade optimal design considering multi-parameters and response surface method. Energies. 2020;13(7):1639–23.
16. Rodriguez CV, Celis C. Design optimization methodology of small horizontal axis wind turbine blades using a hybrid CFD/BEM/GA approach. J Braz Soc Mech Sci Eng. 2022;44(6):254–25.
17. Özkan R, Genç MS. Aerodynamic design and optimization of a small-scale wind turbine blade using a novel artificial bee colony algorithm based on blade element momentum (ABC-BEM) theory. Energy Convers Manag. 2023;283(4):116937–21.
18. Zhu J, Zhou Z, Cai X. Multi-objective aerodynamic and structural integrated optimization design of wind turbines at the system level through a coupled blade-tower model. Renew Energy. 2020;150(1):523–15.

19. Zhu J, Cai X, Gu R. Aerodynamic and structural integrated optimization design of horizontal-axis wind turbine blades. Energies. 2016;9(2):66.
20. Zemamou M, Toumi A, Mrigua K, Lahlou Y, Aggour M. A novel blade design for Savonius wind turbine based on polynomial bezier curves for aerodynamic performance enhancement. Int J Green Energy. 2020;17(11):652–14.
21. Zhang B, Song B, Mao Z, Tian W, Li B, Li B. A novel parametric modeling method and optimal design for Savonius wind turbines. Energies. 2017;10(3):301–20.
22. Maki K, Sbragio R, Vlahopoulos N. System design of a wind turbine using a multi-level optimization approach. Renew Energy. 2012;43(1):101–10.
23. Tang X, Huang X, Peng R, Liu X. A direct approach of design optimization for small horizontal axis wind turbine blades. Procedia CIRP. 2015;36(1):12–5.
24. Belamadi R, Djemili A, Ilinca A, Mdouki R. Aerodynamic performance analysis of slotted airfoils for application to wind turbine blades. J Wind Eng Ind Aerodyn. 2016;151(5):79–99.
25. Kepekci H. Comparative numerical aerodynamics performance analysis of NACA0015 and NACA4415 airfoils. Int J Eng Sci. 2022;2(1):144–8.